Experimental Mechanics (2024) 64:639–653
https://doi.org/10.1007/s11340-024-01055-z

RESEARCH PAPER

Influence of Additional Strut Elements in 3D Re-Entrant Auxetic Unit Cells on the Damage and Energy Absorption Properties

A. C. Kaya[1] · **A. Korucu**[1,2] · **M. Boğoçlu**[2]

Received: 31 July 2023 / Accepted: 4 March 2024 / Published online: 20 March 2024

Abstract

Background Geometric parameter optimization, novel design, and mechanism modeling of auxetic materials have been widely studied. However, manipulating the topology of the 3d printed auxetic unit cells and its influence on the damage have yet to be explored.

Objective This study aims to characterize the energy absorption properties and damage mechanisms of the modified auxetic unit cells.

Methods In the current study, bending-dominated re-entrant auxetic unit cells (Cell0), torsion-dominated auxetic unit cells with cross elements (CellX), buckling-dominated auxetic unit cells with vertical elements (CellB), and bending-dominated auxetic unit cells with panels (CellW) have been fabricated by FDM (Fused deposition modeling). Uniaxial compression testing of the PLA (Polylactic acid) unit cells has been carried out, and a camera has observed their deformation behavior. SR- μCT (Synchrotron radiation microtomography) and an SEM (Secondary electron microscope) accomplished further damage analysis of the struts.

Results Adding additional struts hinders the lateral shrinking of the re-entrant auxetics, and re-entrant auxetic unit cells with cross elements have shown higher energy absorption capacity and efficiency than others. The struts' damage has been governed by building direction, printed material, and strut dimensions. Intra-layer and interlayer fracture of the layers and rupture in the circumferential direction of the PLA struts have been observed in the SR- μCT slices.

Conclusions By additional struts, it is possible to fabricate complex auxetic structures with enhanced energy absorption properties, but their inherent characteristics dominate the damage of the struts in the auxetic unit cells.

Keywords Auxetic materials · Negative poisson's ratio · Compression test · PLA

Introduction

Auxetic foams are unique cellular structures with a negative Poissons' ratio, enabling lateral contraction of material upon compressive loading. This extraordinary material behavior results in enhanced indentation resistance [1], improved sound-damping abilities [2], and increased energy absorption capabilities [3, 4]. Auxetic materials have been exploited in various applications such as stent and orthopedic implant in biomedical applications [5], scaffold in tissue engineering [6], smart material in piezoelectric actuators, helmet in sports protective device, and crash absorber in automobiles [7].

2D hexagonal cellular structures with negative Poisson's ratio were first demonstrated by Gibson et al. [8] in 1982. After that, Lakes [9] created the first 3D re-entrant auxetic unit cells by volumetric compression of the conventional open-cell foams in 1987. The studies regarding auxetic structures focused on the novel design and mechanism modeling of the 2D re-entrant unit cells [10–12], their transformation into 3D patterns [13–15], and geometric parameter optimization for enhanced mechanical properties [16–18]. For instance, Peng and Bargmann [10] proposed a novel hybrid honeycomb structure by merging two hexagonal honeycomb unit cells. Using proper geometric parameters, they further demonstrated that auxetic behavior and

✉ A. C. Kaya
alican.kaya@tau.edu.tr

[1] Mechatronics Engineering Department, Turkish-German University, Sahinkaya Caddesi 86, Beykoz, 34820 Istanbul, Turkey

[2] Construction Division, Department of Mechanical Engineering, Faculty of Mechanical Engineering, Yildiz Technical University, Yildiz, Besiktas, Istanbul 34349, Turkey

stiffness were enhanced for the hybrid honeycomb structure. Furthermore, Cheng et al. [11] showed that the configuration of re-entrant auxetic unit cells with different variable stiffness factors (such as re-entrant angle and strut thickness) resulted in an auxetic structure with tunable stiffness. With increasing development in manufacturing, the transformation of 2D auxetic structures into 3D designs is currently drawing significant attention. For instance, Ren et al. [13] generated 3D buckling-induced brass auxetic materials and fabricated them using 3D printing. They highlighted that auxetic behavior disappeared in the buckling-induced auxetic materials when the base material changed from an elastomer to a ductile metal. Yang et al. [14] fabricated 3D auxetic Ti–6Al–4 V structures by electron beam melting. They reported that the ratio of vertical strut length to the re-entrant strut length significantly influenced the deformation behavior of the auxetic structure. As the geometric parameter of the unit cell significantly affects the auxetic behavior and deformation behavior, studies mainly concentrate on geometric parameter optimizations. For instance, Teng et al. [16] fabricated 3D re-entrant 316L steel honeycomb structures and unit cells and improved energy absorption and compression stiffness by modifying geometric parameters, including length-to-height ratio, radius-to-height ratio, and thickness-to-height ratio using finite element simulation. They concluded that decreasing length and increasing thickness or radius boosted specific energy absorption. Fu et al. [18] proposed a novel 3D auxetic ABS (Acrylonitrile butadiene styrene) structure and tuned re-entrant angles on different faces; they could achieve a negative Poisson's ratio in two orthogonal directions by configuring the design parameters. Bending is the dominant deformation mechanism in the proposed 3D re-entrant auxetic structures, resulting in a stable deformation [14, 16, 17]. Most parametric studies have been studied widely in the literature to achieve better energy absorption properties. Studies regarding manipulating cell structure by adding additional struts/cell walls are rarely found [19, 20].

Additive manufacturing is widely used for the fabrication of complex auxetic structures. Fused deposition modeling (FDM) process parameters and size effects significantly influence the mechanical and deformation behavior of auxetic structures with thin struts [21–24]. Process parameters such as building orientation, layer thickness, infill percentage, and raster angle significantly influence mechanical properties. For instance, decreasing layer thickness increases the strength, and increasing the infill density improves the mechanical properties of the parts [23]. Furthermore, Domingo-Espin et al. [24] revealed that Polycarbonate (PC) parts built up perpendicular to the building layer showed a lower fracture strain. In contrast, PC built up parallel to the building layer exhibited higher strength. Wang et al. [22] highlighted that the fracture mode of the FDM-printed PLA sample was heavily influenced by build orientation. The failure mode is interlayer fracture when the sample aligns to the building layer with an angle less than 45 degrees, and in contrast, the fracture mode of the specimen is intra-layer. Sarvestani et al. [25] conducted low-velocity impact testing on the PLA auxetic sandwich panels fabricated by FDM. They observed delamination between the layers and cracks in the circumferential and radial directions of the panels using X-ray micro-tomography. Hernandez-Contreras et al. [26] carried out a quantification analysis of the anisotropy and voids on the 3D-printed ABS samples using μCT. Furthermore, they developed a correlation between the orientation of the gaps and the mechanical properties of FDM products. In the literature, there is a lack of detailed studies regarding the process-property relationship for additively manufactured auxetic structures.

In the current study, we proposed the insertion of additional struts and cell walls to modify the cell property and control its deformation behavior. For this reason, we fabricated four different 3D PLA auxetic unit cells: i) re-entrant cells, ii) cells with cross element, iii) cells with buckling element, and iv) cells with panels by FDM process. Their deformation behavior was characterized using a uniaxial quasi-static compression test and imaging with a camera. In detail, the damage of the PLA struts was investigated using synchrotron radiated microtomography (SR- μCT) and a secondary electron microscope (SEM). Furthermore, finite element simulation of the unit cells was carried out, and results were validated with experimental results. The energy absorption properties of the unit cells were measured, and possible models for higher energy absorption properties of the auxetics were discussed.

Materials

Filaments

Unmodified and modified re-entrant auxetic unit cells were printed out of silver metallic color Polylactic acid (PLA) filament (Ultimaker, Utrecht, Netherlands). PLA filament has a diameter of about 2.85 ± 0.1 mm, a glass transition temperature of 60 °C, a melting temperature of 145–160 °C, and a density of 1.24 g/cm^3 [27].

Design of Re-entrant Auxetic Cells and Their Modification

Bending-dominated structures have lower structural stiffness than stretch-dominated structures [28]. Maxwell's stability criterion using the number of struts, s, and nodes, n, determines the cell deformation mode in three dimensions as follows [28]:

$$M = s - 3n + 6 \quad (1)$$

If $M < 0$, the deformation mode is bending-dominated. Suppose $M \geq 0$, the deformation mode is stretch-dominated.

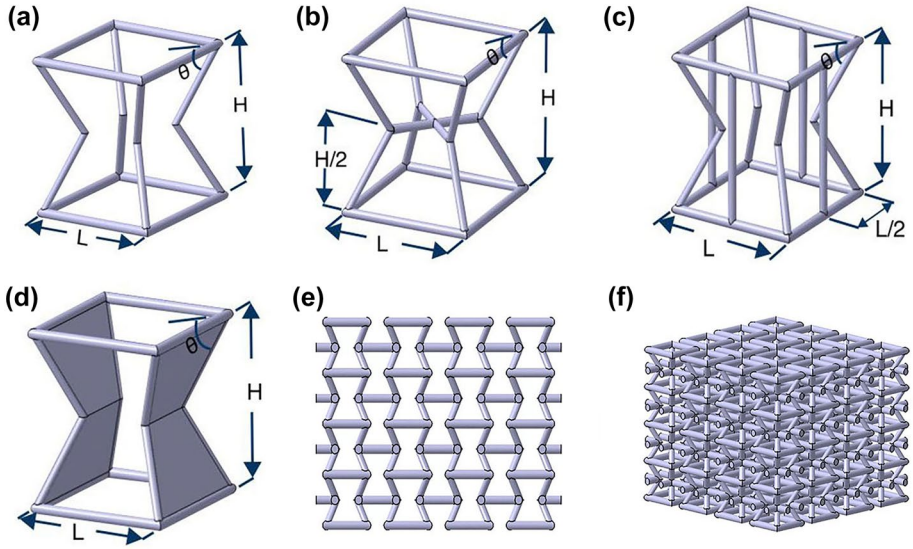

Fig. 1 Design model of four auxetic models: (**a**) bending-dominated re-entrant auxetic cell (Cell0), (**b**) torsion-dominated re-entrant auxetic cells with a cross element (CellX), (**c**) buckling-dominated re-entrant auxetic cell with buckling elements (CellB), and (**d**) bending-dominated re-entrant auxetic cell with panels (CellW). (**e**) 2D and (**f**) 3D pattern models of Cell0

Structures can be buckling-dominated and torsion-dominated depending on the strut thickness, length, and strut orientation concerning the loading axis [29].

In the current study, we created bending-, buckling- and torsion-dominated lattice structures using additional strut and cell wall elements in re-entrant auxetic unit cells to tune and control the mechanical properties of the unit cells. In Fig. 1, a re-entrant auxetic cell (Cell0, bending-dominated), a re-entrant auxetic cell with a cross (X) element (CellX) aligned perpendicular to the loading axis (torsion-dominated), a re-entrant auxetic cell with buckling elements (CellB) aligned parallel to the loading axis (buckling dominated), and a re-entrant auxetic cell with two cell walls (CellW, bending-dominated) deployed on the reciprocal faces are demonstrated. 2D and 3D patterns of Cell0 were demonstrated in Fig. 1(e and f). Dimensions of each unit cell design are shown in Table 1.

Methods

Fabrication Method

Unmodified and modified re-entrant auxetic cells were fabricated by the FDM (Fused deposition modeling, Ultimaker III extended, Utrecht, Netherlands) process. 3D models of re-entrant auxetic cells were generated using CAD (Computer Aided Design) software. CAD data was transformed into the STL file, and subsequently, the G-Code of the specimen was created using slicer software (Cura, Ultimaker, Utrecht, Netherlands). 3D printing parameters of the unit cells are presented in Table 2. Retraction settings were optimized by trial-and-error method. Retraction speed and distance were set to 6.5 mm and 25 mm/s, respectively, to eliminate stringing (SFig. 1). In the current study, all unmodified and modified auxetic cells were fabricated with an infill density of 100% to ensure the stability of the struts. A grid infill pattern and a tree support structure were implemented to print the unit cells.

Table 1 Dimensions of the auxetic unit cells

	Dimension
Height of the cells (H)	50 mm
Length of struts (L)	50 mm
Strut thickness (t)	3 mm
Re-entrant angle (θ)	54.74 degrees

Mechanical Testing

Quasi-static compression tests of the unit cells were conducted with a universal testing machine Shimadzu AGX-V (Kyoto, Japan) outfitted with a load cell of 100 kN possessing a resolution of $\pm 0.5\%$ indicated test force. Auxetic cells were compressed with a strain rate of 10^{-3} s^{-1}

Table 2 Printing parameters of the fabricated auxetic re-entrant unit cells

Parameters	Value
Nozzle Diameter	0.4 mm
Layer Thickness	0.06 mm
Infill Density	100%
Support Type	Tree
Support Branch Distance	1 mm
Bed Temperature	60 °C
Nozzle Temperature	210 °C
Infill Pattern	Grid
Printing Speed	60 m/s

(ASTM D695-15 [30]). The shortening of the auxetic cells was measured from the displacement of the crosshead in the machine. A 2-megapixel CCD camera was utilized to image the sample surface during compression testing to characterize the deformation behavior of unit cells. In the case of tensile testing, a 3D CAD model of the ASTM 638 type II tensile specimen was created using CAD software. CAD models (stl. file format) were imported into the open-source slicer software Cura, and G-Code was generated. The specimen models were placed at 0°, 30°, 45°, and 60° angles to the printer bed and built up with the same printing parameters as unit cells (Table 2). Tensile specimens were pulled with a displacement rate of 5 mm/min (SFig. 2). A video extensometer measured the elongation of the samples. PLA had a nonlinear elastic behavior, and the elastic modulus of the specimens was measured from the tangent modulus as described in ref [31]. At least five and three samples were tested for each unit cell and standard tensile specimen, respectively.

Loading modulus, yield strength, peak stress, and fracture strain were determined from the stress–strain curves of the unit cells. The loading modulus was measured as a slope from the initial loading line in the stress-strain curves. Peak stress is determined as the maximum stress in the stress-strain curves. Fracture strain was determined at strain where a significant stress drop occurs due to the rupture.

The energy absorbed per unit volume, U_v, by the auxetic structure is the area under the stress-strain curve up to the fracture strain, ε_f [32]:

$$U_v = \int_0^{\varepsilon_f} \sigma(\varepsilon) d\varepsilon \tag{2}$$

The energy absorbed per unit mass (U_m) by the auxetic structure is calculated by dividing U_v by cell density (ρ_c).

Energy absorption efficiency, γ, is the ratio between the energy absorbed by an auxetic structure and the energy absorbed by an ideal system [33]. Efficiency is expressed as a percentage:

$$\gamma(\varepsilon) = \frac{\int_0^{\varepsilon} \sigma(\varepsilon) d\varepsilon}{\sigma_{max}(\varepsilon)\varepsilon} * 100 = \frac{Energy\ absorption\ by\ a\ structure}{Energy\ absorption\ by\ an\ ideal\ absorber} \tag{3}$$

Physical properties of auxetic foam structures

The density of the auxetic cells was calculated by dividing the mass of the cells by their volume. As a volume, a cubic shape was assumed. The weight of the sample was measured with a digital microbalance. The volume of the printed auxetic cells was measured with a caliper. The relative density of the cells was calculated by dividing cell density by PLA strut density. The density of the printed PLA strut was measured by Archimedes method ($\rho_s = 1.24 g/cm^3$). A precision microbalance Radwag AS 220.R2 (RADWAG Balances & Scales Radom, Poland) outfitted with a density determination kit was used for the Archimedes method. The readability of this microbalance is 0.1 mg, and the max capacity is 220 gr.

The average measured mass of the cells was divided by the CAD volume of the cells ($53 \times 53 \times 53 mm$) to calculate the cells' theoretical density.

Fracture Observations

Struts in damaged cells were extracted with a side cutter. The struts were mounted upright and fixed by dental composite for scanning by a synchrotron radiation-based X-Ray microtomography (SR-μCT) setup at BAMline of BESSY II [34] of the HZB (Helmholtz Centre Berlin for Materials and Energy, Berlin, Germany). The beam had a parallel geometry and was monochromatic at 24 keV. Struts were imaged with effective pixel resolutions of 1.44 or 3.61 μm. The distance between the specimen and the detector was 100 mm. The reconstruction of the CT data was carried out using an in-house script. A qualitative demonstration of the tomography rendering was conducted using Image J [35] and CT-Voxel (Bruker Corporation, Massachusetts, USA).

Fracture surfaces of the samples were investigated by scanning electron microscope (SEM, Thermo Fisher Quattro ESEM FE-SEM, Waltham, USA). Imaging in the SEM was performed in the secondary electron mode with an accelerating voltage of 2 kV.

FE Modelling

CAD models of auxetic cells were imported into FE software (Abaqus 6.12–2, Dassault Systèmes Simulia Corp., Providence, RI, USA). A 3D volumetric mesh with 4-node linear tetrahedron elements (C3D4) was generated for auxetic and modified cells sized $53 \times 53 \times 53$ mm^3. The different number of elements used for each model ranged from 249,152 to 668,169, which exhibited mesh convergence (Table 3) according to mesh sensitivity study (SFig. 3(a). A reference point coupled with a rigid platen was fixed at one end using tie constraint (SFig. 3b). In contrast, the opposite sample side was associated with a second rigid platen applying compression loading up to a specific displacement for each model (Table 3). General contact was defined using the penalty method with a friction coefficient of 0.15. Only elastic material behavior was assigned based on our tensile test results on standard printed PLA samples (Supplementary Fig. 2). Accordingly, the constitutive material parameters were elastic modulus E = 2461 (MPa, Poisson's ratio μ= 0.325 [36], and density ρ = 1.24 g/cm^3. Two rigid platens were created and meshed with linear

Table 3 Modeling input parameters for compression simulation of the auxetic cells

	Cell0	CellX	CellB	CellW
Number of elements	242,594	268,191	310,300	668,169
Cell displacement (mm)	4	0.78	0.52	3.12

quadrilateral elements of type R3D4. The Poisson's ratio of the auxetic unit cells was measured from a single node at the exterior surface of the struts (marked in Supplementary Fig. 3(c)). The simulation was repeated for each unit cell with a 3-, 6-, and 9-mm strut diameter. A dynamic explicit solver was implemented to assess the quasi-static elastic deformation in the single cells. A quasi-static deformation of the auxetic cells was accomplished within 0.01 s. For elastic models, the kinetic energy of the deformed material was not allowed to exceed 5% of its internal energy throughout the simulation [37].

The axial strain (ε_y), the transverse strain (ε_x) and the Poisson's ratio (ν) of the unit cells were determined by using following equations:

$$\varepsilon_y = \frac{\Delta H}{H_o}, \Delta H = H_o - H_i \tag{4}$$

$$\varepsilon_x = \frac{\Delta B}{B_o}, \Delta B = B_o - B_i \tag{5}$$

$$\nu = -\frac{\varepsilon_x}{\varepsilon_y} \tag{6}$$

where H_o is the initial height and B_o is the initial distance between two points from the exterior surface of the strut (SFig. 3(c)).

Results

3-D Printed Cell Structures

Designed and fabricated auxetic cells differ from each other in the FDM process. The theoretical and measured average densities, measured mass, and measured relative densities of the modified and unmodified auxetic cells are tabulated in Table 4. While the theoretical density of Cell0, CellX, and CellB is higher than the measured cell densities, the theoretical cell density of CellW is lower than the measured cell density. There are remarkable fluctuations in the measured mass of the unit cells, showing that different amounts of material have been deposited at the same volume during printing.

Mechanical Properties

Figure 2(a and b) demonstrate the mean stress–strain and mean normalized (σ/ρ_{rel}) stress–strain curves of the unmodified and modified re-entrant auxetic cells, respectively (Full curves are demonstrated in supplementary SFig. 3). Cells with buckling elements showed the highest strength and the lowest ductility. In contrast, unmodified re-entrant auxetic cells exhibited the lowest strength and the highest elasticity. Cells with cross elements exhibited a short smoothing plateau, while others showed no significant plateau regime, and sudden rupture was observed. Cells with cross elements were stronger than re-entrant auxetic cells and cells with panels. Additional cell walls slightly increased the strength but decreased the fracture strain of the re-entrant auxetic cells.

Cells with a panel showed the highest energy absorption. In contrast, re-entrant auxetic cells exhibited the lowest energy absorption capacity (Fig. 2(c)). Cells with cross elements depicted the highest energy absorption efficiency (Fig. 2(d)). In contrast; they showed a moderate energy absorption capacity due to their lower density as compared to cells with panels. In the case of eliminating the density effect by calculating energy absorption per mass, cells with cross elements showed the highest energy absorption capacity per mass (Table 5). Re-entrant auxetic cells distinctly showed the lowest values for energy absorption capacity per mass.

Deformation Behavior of Cells

At the macroscale, the cell deformation behavior of specimens is demonstrated in Fig. 3 (Supplementary Video 1).

Table 4 Theoretical and measured cell densities

Specimen	Theoretical cell density (g/cm^3)	Measured mass (g)	Measured cell density (g/cm^3)	Measured relative density (%)
Cell0	$3.5*10^{-2}$	4.76±0.08	$3,2±0.06*10^{-2}$	2.6
CellX	$3.7*10^{-2}$	5.14±0.10	$3,5±0.07*10^{-2}$	2.9
CellB	$4.6*10^{-2}$	6.21±0.14	$4.2±0.10*10^{-2}$	3.5
CellW	$9.5*10^{-2}$	14.50±0.11	$9.7±0.08*10^{-2}$	8.2

± indicating standard deviation

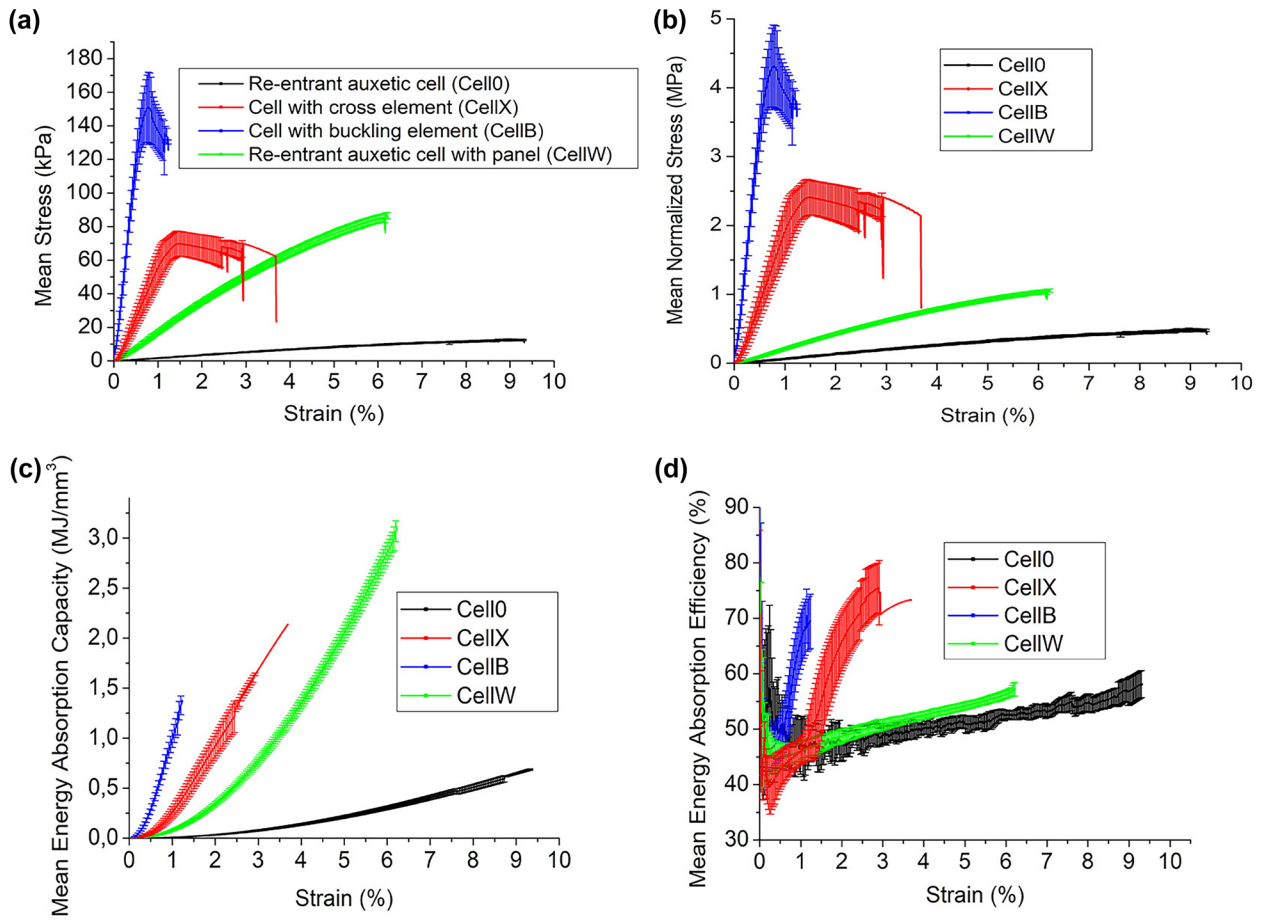

Fig. 2 (**a**) Mean stress-strain and (**b**) mean normalized stress-strain curves of the unmodified and modified unit cells, (**c**) Mean energy absorption capacity versus strain curves, and (**d**) mean energy absorption efficiency versus strain curves

Here, strains corresponding to the values are shown in Fig. 2(a). At a strain of 4% (corresponding to Fig. 2(a), re-entrant auxetic cells (Cell0) underwent elastic deformation. At a strain of 7.5%, corresponding to the fracture strain of the cell, the inner strut failed in the vicinity of the connection point of the inner struts. A white arrow pointed to the fracture point in the re-entrant auxetic cell. In the case of cells with cross elements (CellX), struts failed through torsional elastic deformation at a strain of 1% (Fig. 3(b). At a strain of 2.8%, struts failed by twisting at the connection point of the cross elements and inner struts. In the case of cells with buckling elements, struts were deformed by elastic buckling at a strain of 0.5% (Fig. 3(c). Further loading up to a strain of 1.1%, struts failed catastrophically due to the buckling. In the case of cells with panels, elastic deformation of panels was observed at a strain of 3% (Fig. 3(d). At a strain of 6.2%, cell walls failed at the panels' connection line (white arrow).

Table 5 Average mechanical properties of the unmodified and modified cells

Samples	Elastic modulus (kPa)	Peak stress (kPa)	Fracture strain (%)	Energy absorption capacity (J/mm^3)	Energy absorption per mass (kJ/g)	Energy absorption efficiency (%)
Cell0	165.6 ± 6.8	11.94 ± 0.78	8.56 ± 0.94	0.20 ± 0.04	6.4 ± 1.2	51 ± 2
CellX	11,631.6 ± 2086.8	70.18 ± 7.47	1.54 ± 0.26	0.62 ± 0.20	17.7 ± 5.8	56 ± 4
CellB	25,886.0 ± 2436.5	151.29 ± 20.76	1.23 ± 0.10	0.48 ± 0.08	11.5 ± 1.8	56 ± 4
CellW	1805.4 ± 59.1	85.72 ± 2.72	6.29 ± 0.13	1.07 ± 0.06	11.1 ± 0.6	51 ± 1

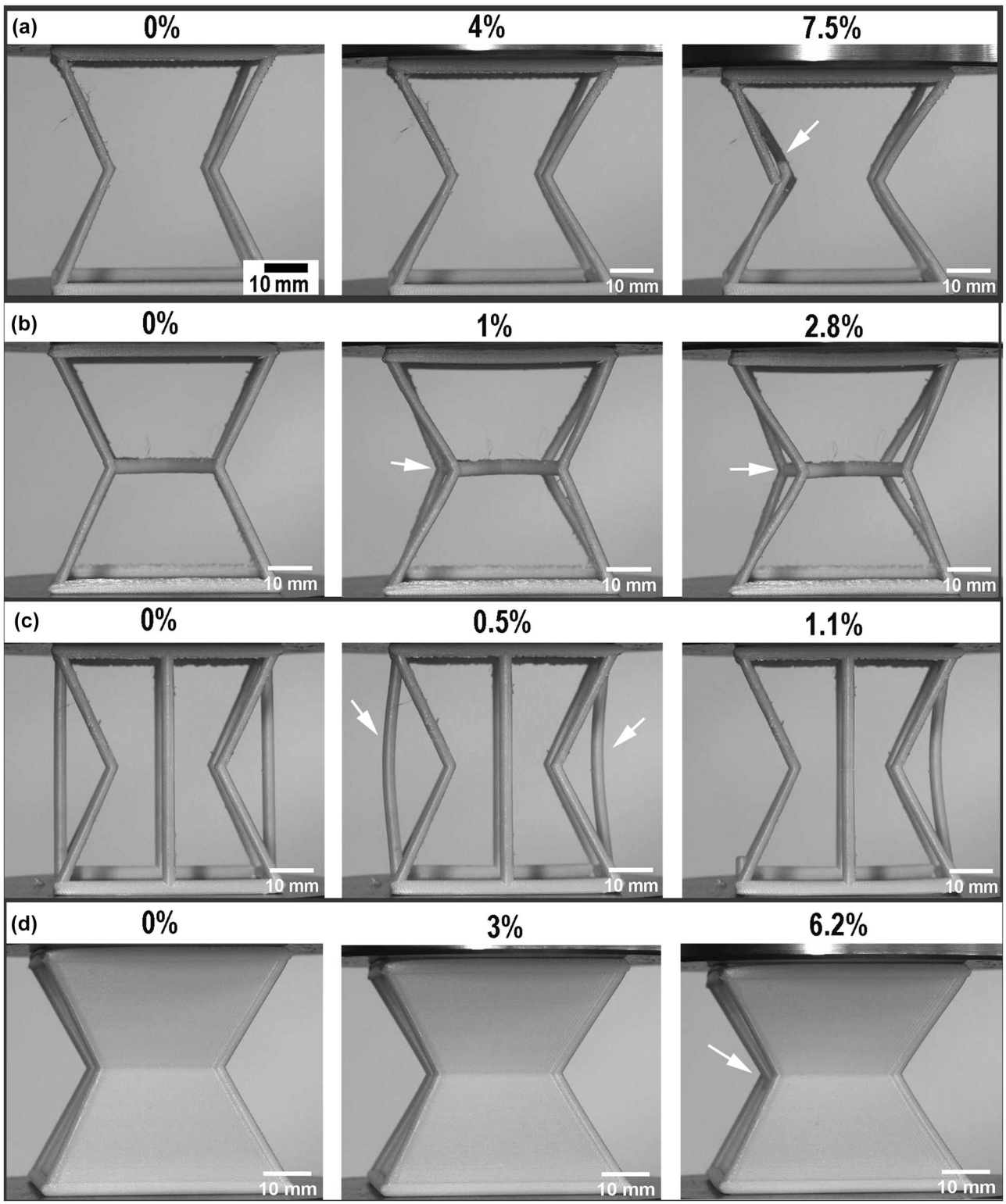

Fig. 3 Figures revealing cell collapse behavior of (**a**) re-entrant auxetic cell at 4 and 7.5% strain, (**b**) cells with cross elements at 1 and 2.8% strain, (**c**) cells with buckling element at 0.5 and 1.1% strain, d) cells with the panel at 3 and 6.2% strain. (**a**) In re-entrant auxetic cells, struts fail at the connection point. The white arrow points to the ruptured strut. (**b**) In the case of cells with cross elements, struts fail through torsion (white arrow). (**c**) Struts failed through buckling, indicated with white arrows. (**d**) Cells with panels failed at the connection point of the panels (white arrow)

Modelling Results

Stress-strain curves from the experiment and FE simulation have well matched each other (Fig. 4). Only the peak stress of the CellB could not be well estimated; the cell with buckling element overestimated the peak stress. The cell with cross-element stress fluctuates after reaching the peak stress, as observed in the experiment. Only cells with panel curves were slightly underestimated by simulation, as seen in Fig. 4(a). When the strut diameter was increased, normalized stress increased substantially in Cell0, CellW, and CellX. However, in the case of CellB, no significant increase was observed up to the strain of 0.008. Over the strain of 0.008, stress drops were observed in the case of CellB with a diameter of 3 mm. Interestingly, CellB with diameters of 6 and 9 did not show any stress drops. Unmodified and modified re-entrant auxetics showed a negative Poisson ratio. There is a scattering in the Poisson's ratio versus strain, as demonstrated in Fig. 4(b). The highest average negative Poisson's ratio was -3.4 for the cell with panel (CellW with D = 3 mm). The average negative Poisson's ratio of Cell0 with a strut diameter of 3 mm was determined to be -1.79. Unit cells with the cross (CellX with d = 3) and buckling (CellB with d = 3 mm) elements exhibited the lowest average negative Poisson ratios (-0.48 and -0.29, respectively). With the increased strut diameter, the negative Poisson's ratio apparently decreased.

Von Mises stress distribution differs for each re-entrant modified and unmodified auxetic structure (Fig. 5). Stress is localized at the connection point of the inner struts in the unmodified re-entrant auxetic cells (Fig. 5(a)). In the case of a cell with cross element, stress concentrates at the connection point of the inner struts and cross elements (Fig. 5(b)). In the cells with buckling elements, stress localized on the lateral side of the strut, and lower stress was observed at the connection point of the inner struts (Fig. 5(c)). In cells with panels, stress concentrates on the connection point of the cell walls (Fig. 5(d)). Further concentration has been observed on the connection point between the struts and the lower and upper part of the cell windows.

Damage Observations in Struts

A brittle fracture of the PLA struts was observed in each cell structure. The delamination and cracking of the inner layers were observed in all fracture surfaces of the struts in modified and unmodified auxetic cells. Red arrows in Fig. 6a–c indicate the pores in the fracture surfaces. The most significant damage and the highest amount of delamination were observed in the buckled struts. Blue dashed lines showed the cracking between the layers on the cell wall.

Using synchrotron μCT, the influence of damage mode on the fracture has been investigated in detail. A 3D rendering of the strut in re-entrant auxetic cells failed by bending was demonstrated in Fig. 7(a). The green square indicated the portion of the sample extracted and scanned. In the longitudinal section of the strut, delamination of the inner layer (intra-layer fracture) underneath the fracture surface becomes visible (Fig. 7(b)). Separation in each layer initiated with micropore formation as seen in Fig. 7(b). A 3D rendering of the connection point of the struts, cut from the cells marked by green square, revealed in Fig. 7(c). Virtual cut is created at the position marked with a blue dashed line. In the cross-section of this virtual cut, rupture of the layer material due to the shear stresses were observed (Fig. 7(d)). Red asterisks indicate the ruptured layer material in the 2D. A buckled strut was extracted

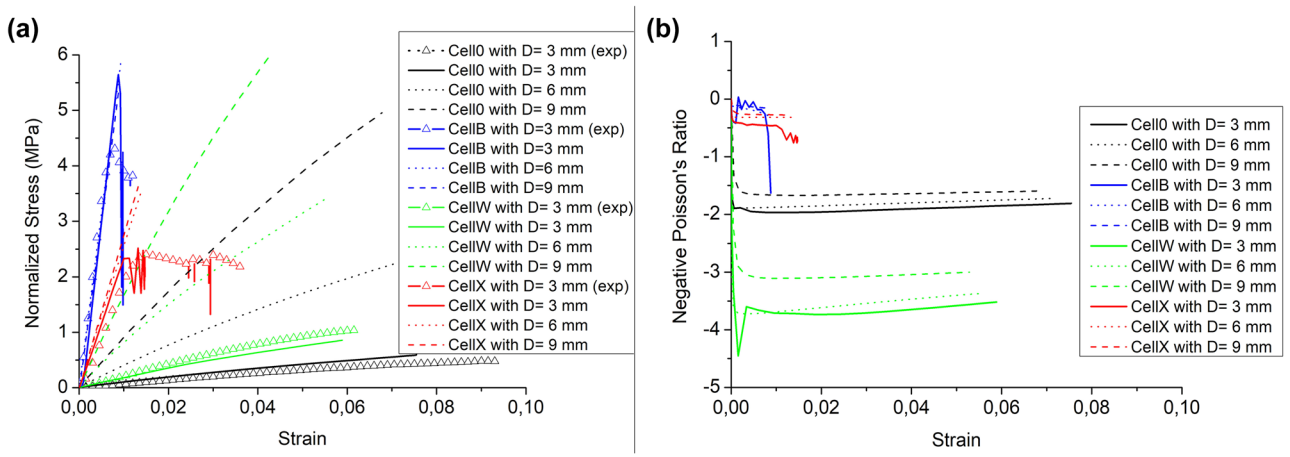

Fig. 4 (**a**) Normalized stress–strain curves from the experimental and simulation results of the re-entrant auxetic cells (Cell0), cells with cross element (CellX), cells with buckling element (CellB), and cells with the panel (CellW) with different strut diameter (D) spanning from 3 to 9. (**b**) Poisson's ratio distribution of unmodified and modified re-entrant auxetics with different strut diameter (D) versus strain

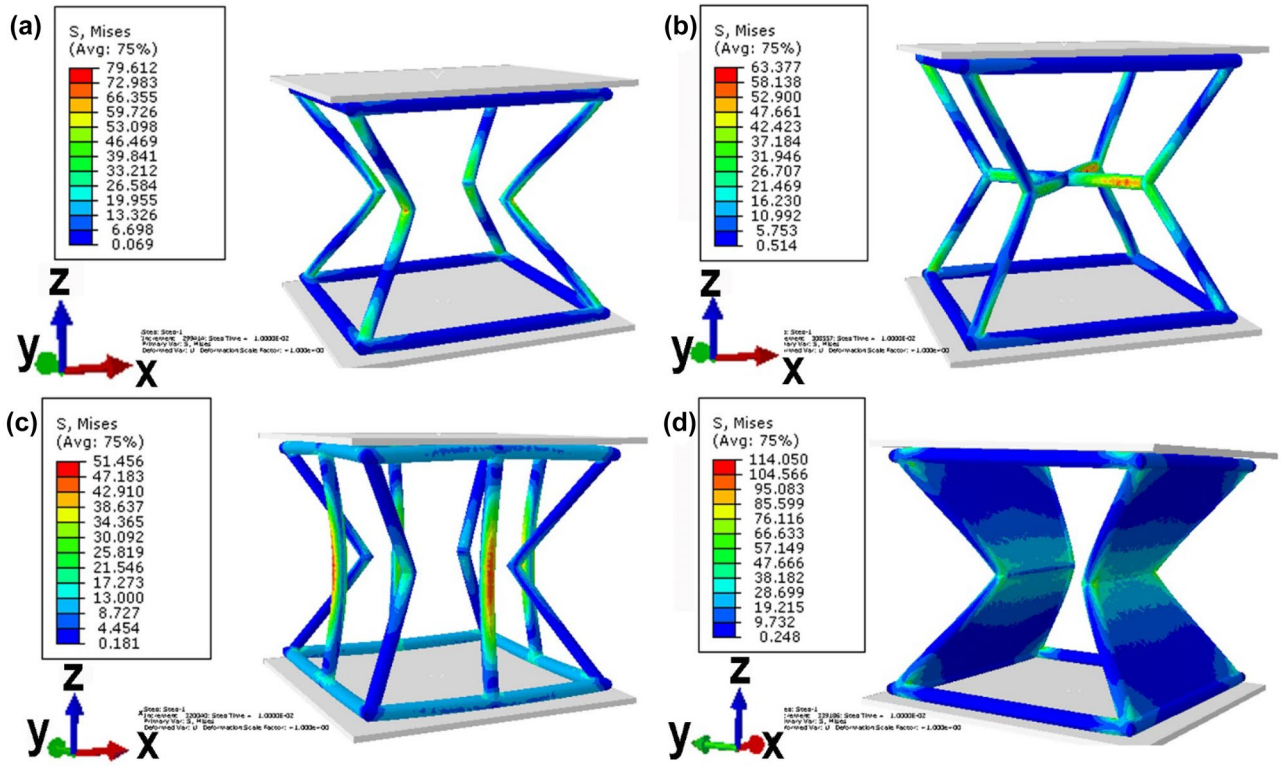

Fig. 5 Von Mises stress distribution in the re-entrant auxetic cells, (**b**) cells with cross element, (**c**) with buckling element, and (**d**) with the panel. (**a**) Stress concentrates mainly on the connection point in the inner strut. (**b**) Stress concentrates in the intersection point of the struts. (**c**) In the buckling element, stress is concentrated in the middle of the strut. (**d**) Stress concentrates in the connection point of the panels

from the geometry marked with a blue square. 3D-rendering of the fracture surface was revealed in Fig. 7(e). A virtual cut from the buckled strut was carried out as indicated by a blue dashed line. In the buckled strut, severe deformation could be observed in the longitudinal section, as demonstrated in Fig. 7(f). There is not only delamination of the layers in parallel to the building direction (red dashed lines) but also there is a delamination of the layers in the perpendicular direction (interlayer fracture) to the building direction (blue arrows).

Discussions

Auxetic Unit Cell Design

Re-entrant auxetic unit cells were modified to control the energy absorption of the auxetic structures. By adjusting the unit cell with additional struts and cell walls, auxetic behavior can disappear. In addition, selected strut material can influence the auxetic behavior of the unit cells. With the expansion of the buckling element, shrinking in the lateral direction was hindered, and the buckling element ruptured due to the brittle behavior of the PLA before the inward shrinking of the re-entrant struts. The study reported that an elastomeric strut material could maintain the auxetic behavior [13]. Furthermore, large deformations could be carried by the unit cell, which was not applied in the current work. In the case of CellX, cross elements retard the shrinking re-entrant struts inward, which lowers the auxetic behavior of the unit cells. After fracture of the re-entrant strut, lateral shrink of the cell can be observed; however, we have not applied large deformations on the unit cells. The reason is that unit cells deform with a very unstable deformation behavior at large deformation (Supplementary Fig. 2). This irregular deformation may be compensated by neighboring cells and strut when the cells are patterned. CellO and CellW showed auxetic behavior as expected. Fabrication of the unit cells by the FDM process was challenging, and therefore, we have chosen those dimensional parameters that enable the fabrication of the unit cells without defects. Parametric studies are not in the scope of the current paper and have not been carried out in this work. We worked on unit cells rather than patterned structures in the present work. Those unit cells are patterned to observe an extended plateau regime for energy absorption applications. In future works, we intend to deal with patterned designs.

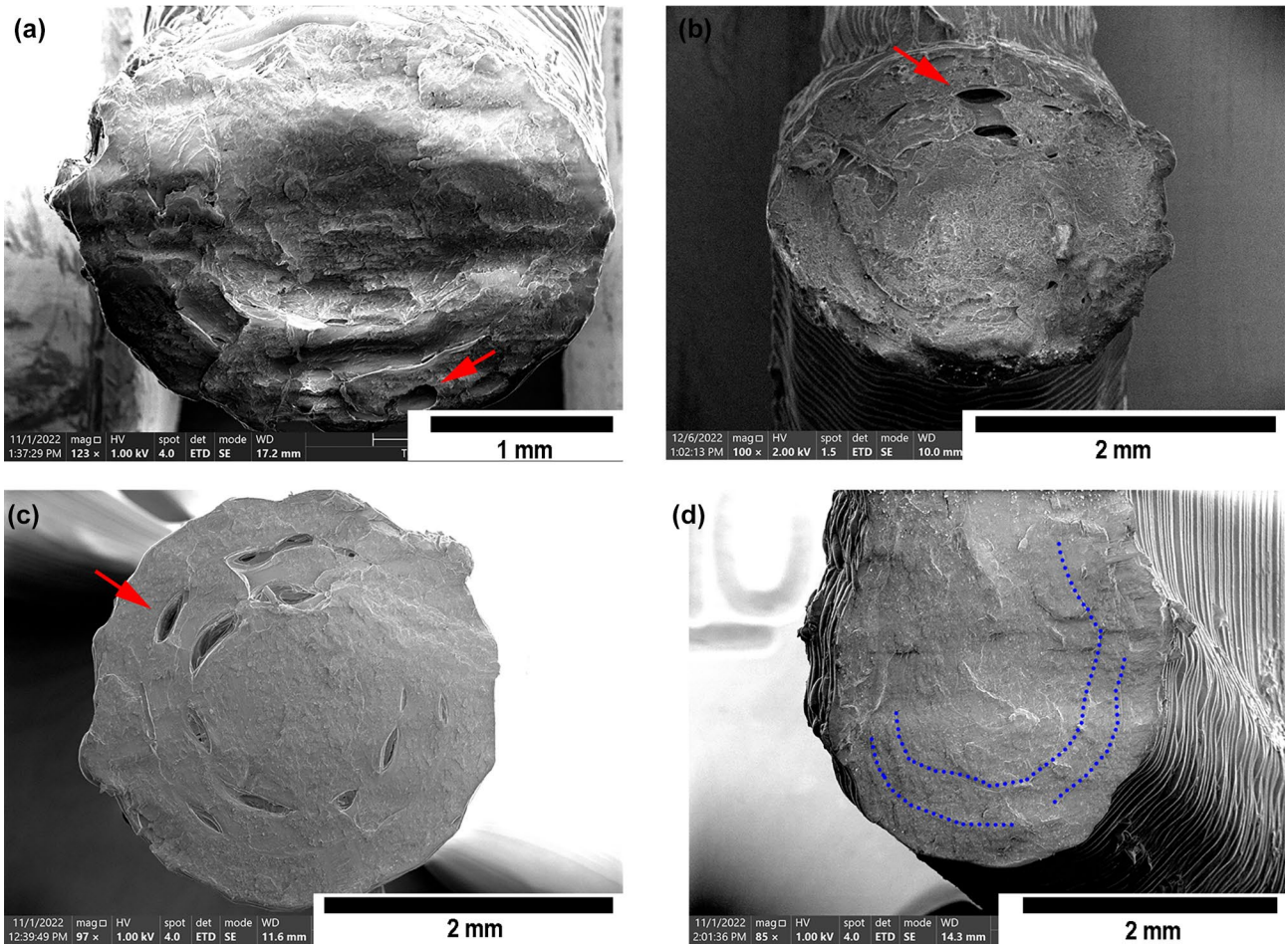

Fig. 6 Fracture surfaces of the struts in the (**a**) re-entrant auxetic cells failed by bending, (**b**) cells with cross element failed by torsion, (**c**) cells with buckling element failed by buckling, and panel in the **d** cells with the panel failed by bending. Red arrows point to the pore formation in the interface between the print layers in (**a**, **b**, and **c**). In the fracture surface of the panel, dashed blue lines indicate the cracks in the interface between the print layers

Effects of Additional Struts and Walls on the Mechanical Properties

Mechanical properties of the developed unit cells were governed here by the cell structure. By modification of the cell structure by buckling and cross elements, strength was increased, and peak stress was followed by strain softening. Effects of increasing auxetic structure density due to the additional struts and panels on the mechanical properties are negligible according to the normalized stress–strain curves (Fig. 2(b). CellW showed a higher strength than Cell0. This can be attributed to the stretching of the panels, which increases the stiffness and stability of the unit cell.

The energy absorption property of the unit cells is heavily influenced by stiffness, strength, and fracture strain. Cell0 and CellW showed higher fracture strain than others; however, their stiffness and strength are lower than others. For energy absorption properties, stiffness and strength are the dominating factors when the difference in strength is enormous. Therefore, CellX has the highest energy absorption capacity per mass and high efficiency. Energy absorption efficiency depends on the unit cells' stress–strain curve shapes. Stiffness, the strength of unit cells, and the flatness of the plateau regime are essential parameters in energy absorption efficiency [38].

The Poisson's ratio is a maximum of -4 for the CellW, consistent with the analytical and experimental measurement in the study reported by Subramani et al. [39]. Subramani et al. [39] further demonstrated that the Poisson's ratio changed with re-entrant angle: Poisson's ratio of auxetic structure spanned from -4.57 to -7.05 at angles between 74.5 and 85 degrees. The Poissons' ratio concerning the strain fluctuated due to the change in the lateral shrinking. Movement of the inner struts inward during compression influences the re-entrant angles, modifying lateral shrinking. Unit cells with panels showed the highest energy absorption

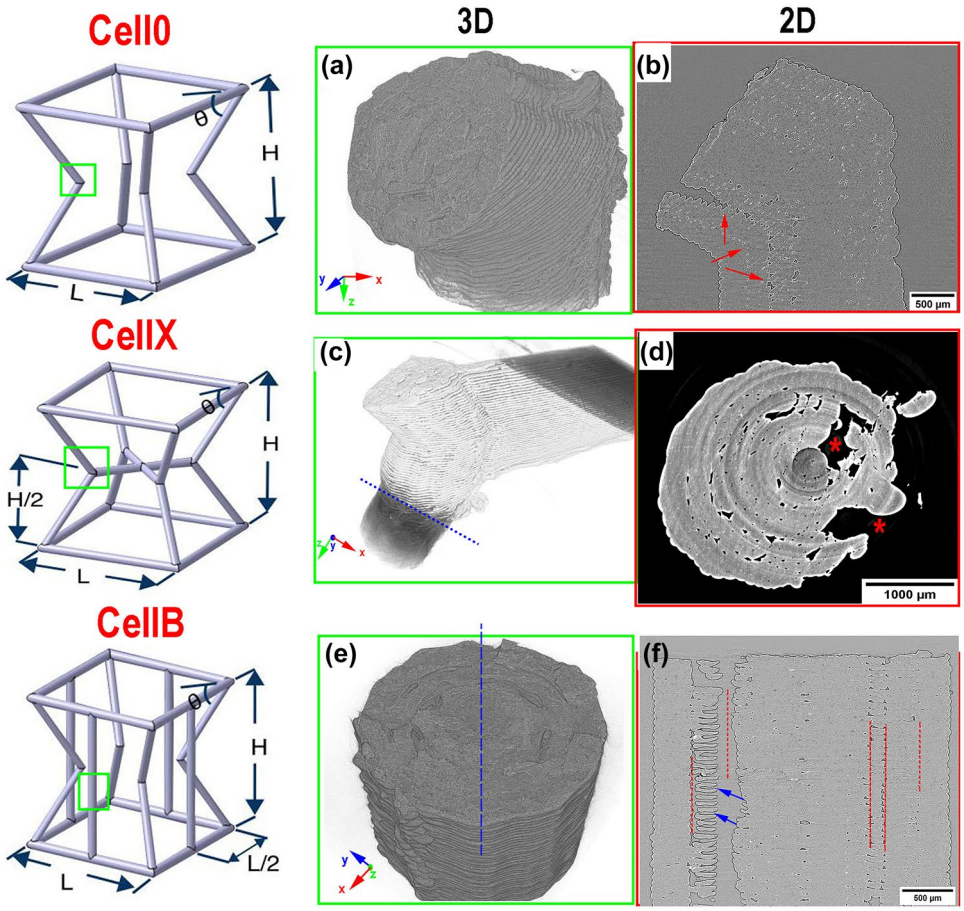

Fig. 7 3D rendering and 2D synchrotron μCT slice of the struts extracted from compressed unit cells. (**a**) A 3D rendering of bent struts in Cell0 reveals that printing layers are tilted with an acute angle. (**b**) Red arrows point to the delamination of the printing layers (intra-layer fracture) due to the bending. (**c**) Node in the connection point of the three struts are highlighted by 3D rendering. Printing layers have various orientations for each strut. (**d**) Strut cross-section virtually cut from the CT slice (blue dashed line, d) Red asterisks "*" point to the circumferential rupture of the deposited material by shear forces. (**e**) The 3D rendering of the buckling element demonstrates a fracture surface. (**f**) The longitudinal section of the buckling element was demonstrated by the virtual cut from the CT slice (blue dashed line, (**f**). Red dashed lines point to the delamination of the printing layers in the parallel direction (intra-layer fracture) to the building direction, and blue arrows point to the delamination of the printing layers in the perpendicular direction (interlayer fracture) to the building direction

capacity with the highest negative Poisson's ratio. The highest negative Poisson ratio indicates lateral shrinking is more significant, improving energy absorption capacity by hindering axial compaction.

Damage Behavior of Modified Auxetic Cells

Damage behavior in the struts was heavily influenced by several parameters, including the orientation of the struts to the building direction, strut dimensions, and material used in the FDM process. The orientation of the struts and their connection with the neighboring struts determine the deformation mode of the struts, such as twisting and buckling mechanisms of the additional struts in the CellX and CellB. The slenderness ratio is an essential parameter for critical stress (σ_{cr}) developed in the buckling element.

$$\sigma_{cr} = \frac{\pi^2 E}{(L/k)^2} \tag{7}$$

where L/k is the slenderness ratio, E is the elastic modulus, L is the strut length, and k is the radius of gyration (d/4 for circular cross-section) [40]. In our design, the slenderness ratio is 66.67, and critical stress is calculated to be 5.3 MPa, which is relatively lower than the yield strength of the struts (~20 MPa), leading to the fracture of the struts due to the buckling. Our findings are consistent with the results of Torre et al. [41]. They demonstrated that buckling occurs in 3D-printed PLA specimens when the slenderness ratio exceeds 9.5. They measured the yield stress at about 60 MPa, and the critical stress was around 50. In our study, with diameters increasing to 6 and 9 mm, the slenderness ratio decreased to 29.33 and 18.22, and critical stress increased to 28.2 and

73.2 MPa, respectively. In the case of CellB with diameters of 6 and 9, buckling is not expected, and struts fail by compression deformation (yielding at about 20 MPa). Therefore, we did not observe a stress drop over a strain of 0.008 for the unit cells with strut diameters of 6 and 9 mm (Fig. 4(a)).

In the case of CellX, the twisting angle is directly proportional to the re-entrant strut length and inversely proportional to the fourth power of the strut radius. PLA is sensitive to shear deformation due to its lower shear strength (~ 11 MPa [42]) than yield strength. Therefore, CellX has a lower fracture strain than Cell0 and CellW. Increasing the strut diameter obstructs the twisting, and struts tend to fail by compression.

Increasing the strut diameter of the auxetic unit cells improved their mechanical properties. Cell0 and CellW mainly fail by bending due to the re-entrant struts/walls, and the second moment of inertia increases by diameter, increasing the bending stiffness. The compressive stresses dominate the unit cell deformation in the case of Cell0 and CellW with large diameters (> 3 mm).

In the damage of the 3D printed struts, intra-layer, inter-layer fracture of the layers, and rupture of the deposited material have been investigated (Figs. 6 and 7). In the case of struts, fractures of the deposited material and layers become visible; cracks have been observed in the case of panels. Panels have large cross-sections, and the number of layers and deposited material in the cross-section is more significant than the struts. Moreover, the panels have a higher moment of inertia than the struts; therefore, damage to the panels is minor (Fig. 6(d)). A sketch representing the damage modes in the unmodified and modified auxetic unit cells is given in Fig. 8.

In the case of unit-cell design, various design parameters could be controlled easily; however, in the FDM process, there are essential characteristics such as layers, building direction, constraints in design for printing, and limits in material selection. Those features greatly influence the damage and mechanical properties of the struts and unit cells. For instance, Kiendl and Gao [43] demonstrated that alternating raster layers built up symmetrically about the loading axis improved the strength and toughness of the materials. These proposed raster layups also inhibit the delamination of the deposited materials. However, in our case, the strut thickness was 3 mm, which was relatively small, and raster mode could not be applied due to the small cross-section. Furthermore, the damage and deformation in the patterned structure can be different due to the influence of the neighboring cells, which will be investigated in our future work.

Theoretical and measured cell densities differed due to the thermal expansion and contraction during printing. In the case of CellW, the measured cell density was higher than the theoretical density, while the theoretical density was higher for the others. More material was deposited in the panels than in struts; therefore, cell volume expansion could occur lower than in others.

Imperfection and Anisotropy in the Printed Struts

Our experimental results match the simulation results well. Deformation behavior and stress–strain curves were successfully reproduced. However, slight differences in the peak stress and fracture strain have been revealed. Fabrication features and defects in the models created by CAD software are not considered (Fig. 9). Those defects are summarized as i) warping of the unit cell bottom (Fig. 9(a), ii) surface waviness on the re-entrant strut edge (white arrow depicting in the Fig. 9(b), and iii) notches on the strut edge (red arrow point to the notch in Fig. 9(c). Warping occurs due to the cooling and shrinking of the deposited material. Surface waviness is observed in poor machine performance, vibration during printing, inadequate adhesion between the layers, thermal deviations, and insufficient support materials [44]. Removing the supports leads to micro notches on the strut surfaces. Therefore, the influence of process parameters and their characteristic features can lead to a difference between the experimental and simulation results. According to the literature, Xu et al. [45] and Albertini et al. [46] also observed overestimation in the simulation results compared to experimental results, as in our results. When the specimens are built up with different print angles, mechanical properties

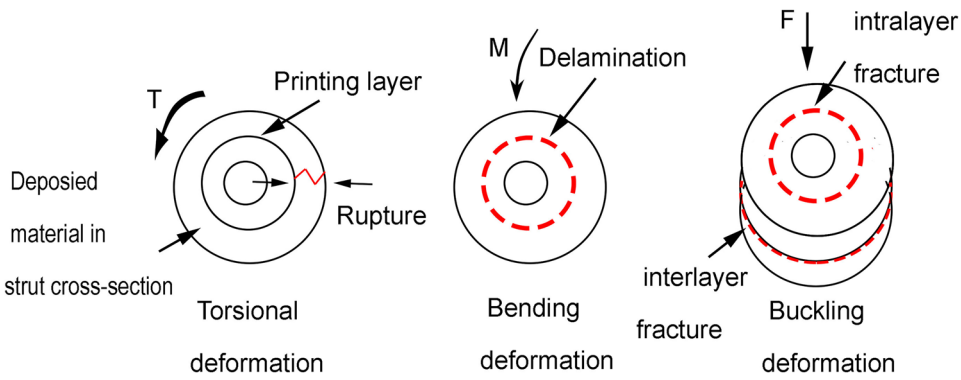

Fig. 8 A sketch represents the deformation modes on the 3D printed struts in the modified auxetic unit cells

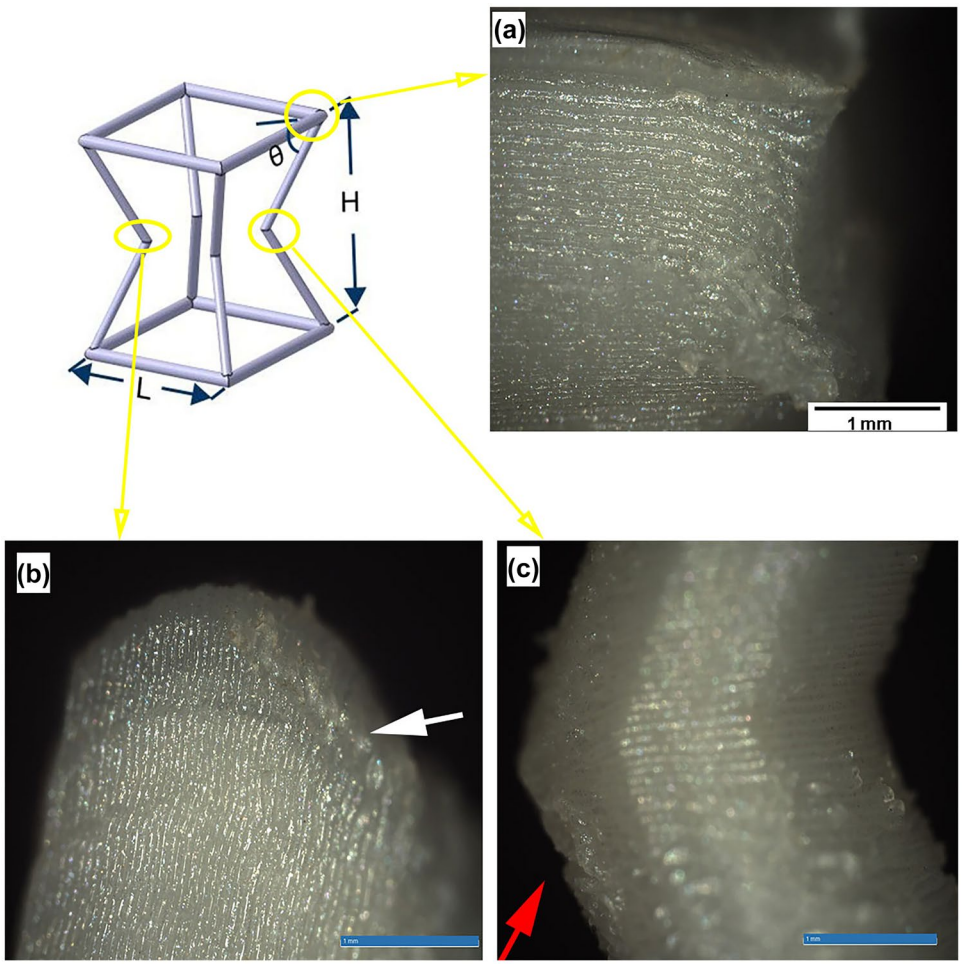

Fig. 9 Fabrication defects in the unit cells: (**a**) warping on the bottom of the unit cells, (**b**) surface waviness on the re-entrant strut edge (white arrow), and (**c**) notches on the strut edge (red arrow)

differ (SFig. 2), posing a significant issue in determining the constitutive material properties of the unit cells [47, 48]. The strength of the printed sample decreased with increasing the print angle. A sample with a 90^{o} degree print angle could not be produced because the fiber had friction with the formerly deposited layers at small layer thickness, leading to movement of the part, resulting in printing stringing and errors. We, therefore, built up a standard specimen that was tilted 60 degrees as re-entrant struts and only elastic properties were considered, as in the study [45]. Moreover, struts have a small dimension, where the size effect can influence the mechanical properties of the struts [21]. This difference can be compensated in patterned structures due to the large number of struts and cells. In our future work, we will investigate those open questions for clarity.

Conclusions

In the current study, we fabricated four different auxetic unit cells using the FDM process: i) re-entrant auxetic structures (Cell0), ii) auxetic cells with cross elements (CellX), iii) auxetic unit cells with bucking elements (CellB) and iv) auxetic unit cells with panels (CellW). We performed compression testing for deformation and damage analysis of the cells and struts. Detailed investigation of the damage was conducted by SEM and SR- µCT. Significant findings in the current study can be summarized in the following:

1. Intra-layer and interlayer fracture of layers and rupture in the circumferential direction of the PLA struts have been observed in the SR- µCT slices. The damage was dominated by the orientation of the struts concerning building direction, printed material, and strut dimensions.
2. CellX shows a remarkable strength with acceptable fracture strain, resulting in a higher energy absorption per mass and efficiency than Cell0 and CellW. CellB shows the highest strength but very low fracture strain. By selecting an elastomer, energy absorption properties can be boosted.
3. In the elastic deformation, additional struts in CellX and CellB obstruct lateral shrinkage of the unit cell. Upon further loading, lateral shrinkage occurs after the re-entrant or vertical struts rupture.

4. The orientation of the struts in each unit cell is different, and the building direction in the FDM process governs their mechanical properties. Therefore, determining the constitutive material parameters for unit cells is challenging.
5. Panels in the unit cells have a high second moment of inertia, resulting in higher strength and higher energy absorption properties of CellW than re-entrant auxetic cells (Cell0).

Supplementary Information The online version contains supplementary material available at https://doi.org/10.1007/s11340-024-01055-z.

Acknowledgements Ali Can Kaya gratefully acknowledges Prof. Claudia Fleck (Materials Engineering, TU Berlin) for her outstanding support, help, and valuable discussions during synchrotron tomography measurements and for the use of the FE Software (Abaqus 6.12-2 (Dassault Systèmes Simulia Corp., Providence, RI, USA). This study was supported by the Turkish–German University Scientific Research Projects Commission under grant no: 2022BM01. We are thankful for the excellent support of Paul Zaslansky (Charité-Universitätsmedizin Berlin), Henning Markötter, and Michael Sintschukand for beamtime access to the BAMline imaging beamline of BESSY II, Helmholtz Zentrum Berlin (HZB).

Funding Open access funding provided by the Scientific and Technological Research Council of Türkiye (TÜBİTAK). Ali Can Kaya reports Turkish-German University provided financial support.

Data Availability The raw/processed data required to reproduce these findings cannot be shared at this time as the data also forms part of an ongoing study.

Declarations

Competing of Interest The authors declare no competing interests.

References

1. Lakes RS, Elms K (1993) Indentability of conventional and negative poisson's ratio Foams. J Compos Mater 27:1193–1202
2. Ruzzene M, Mazzarella L, Tsopelas P, Scarpa F (2002) Wave propogation in sandwich plates with periodic auxetic core. J Intel Mat Syst Str 13:587–597
3. Bezazi A, Scarpa F (2007) Mechanical behaviour of conventional and negative poisson's ratio thermoplastic polyurethane foams under compressive cyclic loading. Int J Fatigue 29:922–930
4. Scarpa F, Pastorino P, Garelli A, Patsias S, Ruzzene M (2005) Auxetic compliant flexible PU foams: static and dynamic properties. Phys Status Solidi (B) 242:681–694
5. Ruan XL, Li JJ, Song XK, Zhou HJ, Yuan WX, Wu WW, Xia R (2018) Mechanical design of antichiral-reentrant hybrid intravascular stent. Int J Appl Mech 10:1850105. https://doi.org/10.1142/S1758825118501053
6. Jin Y, Xie C, Gao Q, Zhou X, Li G, Du J, He Y (2021) Fabrication of multi-scale and tunable auxetic scaffolds for tissue engineering. Mater Design 197:109277
7. Wilt JK, Yang C, Gu GX (2020) Accelerating auxetic metamaterial design with deep learning. Adv Eng Mater 22:1901266
8. Gibson LJ, Ashby MF, Schajer GS, Robertson CI (1982) The mechanics of two-dimensional cellular materials. Proc R Soc Math 382:25–42
9. Lakes R (1987) Foam structures with a negative poisson's ratios. Science 235:1038–1040
10. Peng XL, Bargmann S (2021) A novel hybrid-honeycomb structure: enhanced stiffness, tunable auxeticity and negative thermal expansion. Int J Mech Sci 190:106021
11. Cheng X, Zhang Y, Ren X (2022) Design and mechanical characteristics of auxetic metamaterial with tunable stiffness. Int J Mech Sci 23:107286
12. Ai L, Gao XL (2018) An analytical model for star-shaped re-entrant lattice structures with the orthotropic symmetry and negative poisson's ratios. Int J Mech Sci 145:158–170
13. Ren X, Shen J, Ghaedizadeh A, Tian H, Xie YM (2015) Experiments and parametric studies on 3D metallic auxetic metamaterials with tuneable mechanical properties. Smart Mater Struct 24:95016
14. Yang L, Harrysson O, West H, Cormier D (2012) Compressive properties of Ti– 6Al–4V auxetic mesh structures made by electron beam melting. Acta Mater 60:3370–3379
15. Lvov VA, Senatov FS, Korsunsky AM, Salimon AI (2020) Design and mechanical properties of 3D-printed auxetic honeycomb structure. Mater Today Comm 24:101173
16. Teng XC, Ren X, Zhang Y, Jiang W, Pan Y, Zhang XG, Zhang XY, Xie YM (2022) A simple 3D re-entrant auxetic metamaterial with enhanced energy absorption. Int J Mech Sci 229:107524
17. Yang L, Harrysson O, West H, Cormier D (2015) Mechanical properties of 3D re-entrant honeycomb auxetic structures realized via additive manufacturing. Int J Solids Struct 69–70:475–490
18. Fu M, Chen Y, Zhang W, Zheng B (2016) Experimental and numerical analysis of a novel three-dimensional auxetic metamaterial. Phys Status Solidi B 253:1565–1575
19. Ma Q, Rejab MRM, Siregar JP, Guan Z (2021) A review of the recent trends on core structures and impact response of sandwich panels. J Compos Mater 55:1–43
20. Bronder S, Herter F, Röhrig A, Jung A (2022) Design study for multifunctional 3D re-entrant auxetics. Adv Eng Mater 24:2100816
21. Kaya AC, Salamci MU, Fleck C (2023) Influence of anisotropy on the deformation behaviour in microtensile 316L steel specimens fabricated by laser powder bed fusion (PBF-LB/M). Mater Sci Eng A 863:144521
22. Wang S, Ma Y, Deng Z, Zhang S, Cai J (2020) Effects of fused deposition modeling process parameters on tensile, dynamic mechanical properties of 3D printed polylactic acid materials. Polym Test 86:106483
23. Popescu D, Zapciu A, Amza C, Baciu F, Marinescu R (2018) FDM process parameters influence over the mechanical properties of polymer specimens: a review. Polym Test 69:157–166
24. Domingo-Espin M, Puigoriol-Forcada JM, Garcia-Granada A-A, Llumà J, Borros S, Reyes G (2015) Mechanical property characterization and simulation of fused deposition modeling polycarbonate parts. Mater Des 83:670–677

25. Sarvestani HY, Akbarzadeh AH, Niknam H (2018) Hermenean, 3D printed architected polymeric sandwich panels: energy absorption and structural performance. Compos Struct 200:886–909
26. Hernandez-Contreras A, Ruiz-Huerta L, Caballero-Ruiz A, Moock V, Siller HR (2020) Extended CT void analysis in FDM additive manufacturing components. Mater 13(17):3831
27. Ultimaker PLA (2018) Technical data sheet. Version 4:002
28. Ashby MF (2006) The properties of foams and lattices. Phil Trans R Soc A 364:15–30
29. Gibson LJ, Ashby M (1997) Cellular solids: structure and Properties, 2nd edn. Cambridge University Press, Cambridge, United Kingdom
30. ASTM D695-15 (2023) Standard test method for compressive properties of rigid plastics. https://doi.org/10.1520/D0695-23
31. ASTM E 111–97 (2017) Standard test method for Young's Modulus, Tangent Modulus, and Chord Modulus. https://doi.org/10.1520/E0111-17
32. Paul A, Ramamurty U (2000) Strain rate sensitivity of a closed-cell aluminum foam. Mater Sci Eng A281:1–7
33. Thornton PH, Magee CL (1975) The deformation of aluminum foams. Metall Trans A 6A:1253–1263
34. Rack A, Zabler S, Müller BR, Riesemeier H, Weidemann G, Lange A, Goebbels J, Hentschel M, Görner W (2008) High resolution synchrotron-based radiography and tomography using hard X-rays at the BAMline (BESSY II). Nucl Inst Methods a 586:327–344
35. Abramoff MD, Magelhaes PJ, Ram SJ (2004) Image Processing with ImageJ. Biophotonics Int 11:36–42
36. Ferreira RTL, Amatte IC, Dutra TA, Bürger D (2017) Experimental characterization and micrography of 3D printed PLA and PLA reinforced with short carbon fibers. Compos Part B Eng 124:88–100
37. Kader MA, Islam MA, Saadatfar M, Hazell PJ, Brown AD, Ahmed S, Escobedo JP (2017) Macro and micro collapse mechanisms of closed-cell aluminium foams during quasi-static compression. Mater Des 118:11–21
38. Kaya AC, Zaslansky P, Ipekoglu M, Fleck C (2018) Strain hardening reduces energy absorption efficiency of austenitic stainless steel foams while porosity does not. Mater Des 143:297–308
39. Subramani P, Rana S, Ghiassi B, Fangueiro R, Oliveira DV, Lourenco PB, Xavier J (2016) Development and characterization of novel auxetic structures based on re-entrant hexagon design produced from braided composites. Compos Part B Eng 93:132–142
40. Hibbeler RC (2013) Technische mechanik/2 - Festigkeitslehre. Pearson, München
41. Torre R, Brischetto S, Dipietro IR (2021) Buckling developed in 3D printed PLA cuboidal samples under compression: analytical, numerical and experimental investigations. Addit Manuf 38:101790
42. Reverte JM, Caminero MÁ, Chacón JM, García-Plaza E, Núñez PJ, Becar JP (2020) Mechanical and geometric performance of PLA-based polymer composites processed by the fused filament fabrication additive manufacturing technique. Mater 13:1924
43. Kiendl J, Gao C (2020) Controlling toughness and strength of FDM 3D-printed PLA components through the raster layup. Compos Part B: Eng 180:107562
44. Golhin AP, Tonello R, Frisvad JR, Grammatikos S, Strandlie A (2023) Surface roughness of as-printed polymers: a comprehensive review. Int J Adv Manuf Tech 127:987–1043
45. Xu Y, Zhang H, Šavija B, Figueiredo SC, Schlangen E (2019) Deformation and fracture of 3D printed disordered lattice materials: experiments and modeling. Mater Design 162:143–153
46. Frédéric Albertini J, Dirrenberger C, Sollogoub T, Maconachie M, Leary A, Molotnikov (2021) Experimental and computational analysis of the mechanical properties of composite auxetic lattice structures. Additive Manuf 47:102351
47. Seibert P, Susmel L, Berto F, Kästner M, Razavi SMJ (2021) Applicability of strain energy density criterion for fracture prediction of notched PLA specimens produced via fused deposition modeling. Eng Fract Mech 258:108103
48. Marșavina L, Vălean C, Mărghitaș M, Linul E, Razavi SMJ, Berto F, Brighenti R (2022) Effect of the manufacturing parameters on the tensile and fracture properties of FDM 3D-printed PLA specimens. Eng Fract Mech 274:108766